

Slow Light Nanocoatings for Ultrashort Pulse Shaping

M. Ossiander^{1,*}, Y.-W. Huang¹, W.T. Chen¹, Z. Wang², X. Yin¹, Y. A. Ibrahim^{1,3}, M. Schultze², F. Capasso^{1,*}

¹ John A. Paulson School of Engineering and Applied Sciences, Harvard University, 29 Oxford St, Cambridge, MA 02138, United States

² Institute of Experimental Physics, Graz University of Technology, Petersgasse 16, 8010 Graz, Austria

³ University of Waterloo, Waterloo, ON N2L 3G1, Canada

* Corresponding Authors: mossiander@g.harvard.edu, capasso@seas.harvard.edu

Transparent materials do not absorb light but have profound influence on the phase evolution of transmitted radiation. One consequence is chromatic dispersion, i.e., light of different frequencies travels at different velocities, causing ultrashort laser pulses to elongate in time while propagating. Here we experimentally demonstrate ultrathin nanostructured coatings that resolve this challenge: we tailor the dispersion of silicon nanopillar arrays such that they temporally reshape pulses upon transmission using slow light effects and act as ultrashort laser pulse compressors. The coatings induce anomalous group delay dispersion in the visible to near-infrared spectral region around 800 nm wavelength over an 80 nm bandwidth. We characterize the arrays' performance in the spectral domain via white light interferometry and directly demonstrate the temporal compression of femtosecond laser pulses. Applying these coatings to conventional optics renders them ultrashort pulse compatible and suitable for a wide range of applications.

Femtosecond light pulses are the basis for the highest achievable time resolutions and electrical field intensities today and have become central tools in microscopy¹, medicine², technology³, and physical chemistry⁴. A key challenge in their application remains dispersion control: Because all transparent materials are normally dispersive in the ultraviolet, visible, and near-infrared regions below a wavelength of 1.3 μm , the realization of compressed laser pulses currently requires complex angular dispersive⁵⁻⁷, reflective⁸⁻¹⁰, or photonic-crystal-fiber-based compression setups¹¹. Recently, dielectric metasurfaces, in addition to their use as lenses and for spatially shaping the phase and polarization of light on the nanoscale¹²⁻¹⁵, were employed in an angular-dispersive Fourier-transform setup¹⁶, providing fine-grained control of the time-domain properties of ultrashort laser pulses.

In this work, we demonstrate ultrathin nanocoatings that induce anomalous group delay dispersion directly upon transmission. The approach is illustrated in Fig. 1a: the nanocoatings can straightforwardly be applied to conventional optics and compensate their group delay dispersion or be implemented in existing laser setups to compress ultrashort laser pulses. As such, the coatings can

simplify the use and expand the applicability of femtosecond laser pulses. Therefore, they can act as the basis for a new array of anti- or non-dispersive optics. Compared to theoretically proposed approaches based on plasmonics¹⁷ or flat nanodisk Huyghens metasurfaces¹⁸, our high-aspect-ratio nanopillar coating combines high transmission, anomalous dispersion, low high-order dispersion, and broadband operation.

The influence of transmissive optics on the time-domain profile of ultrashort laser pulses can be quantified by the frequency-dependent group delay $GD = \frac{d\varphi}{d\omega}$, which is calculated as the derivative of the angular-frequency-dependent spectral phase $\varphi(\omega)$ imprinted by the optics. Visible and near-infrared ultrashort laser pulses transmitted through transparent optics elongate because the pulses' high frequency (blue) components are delayed more than their low frequency (red) components, i.e., $GD(\omega_{red}) < GD(\omega_{blue})$. Far from resonances, most materials' group delay profiles are approximately linear, thus, they are approximated by their positive slope, the group delay dispersion $GDD = \frac{dGD}{d\omega} = \frac{d^2\varphi}{d\omega^2} > 0$. To compensate for the temporal broadening of ultrashort pulses upon transmission through optical elements, our goal is to create a coating with the opposite effect, i.e., $GD(\omega_{red}) > GD(\omega_{blue})$ or $GDD < 0$.

Our nanocoating consists of uniform circular amorphous silicon nanopillars arranged in a periodic square array (see Fig. 1b). We identify promising design parameters (nanopillar diameter, height, and periodicity) by exploring a large parameter space using rigorous coupled-wave analysis (RCWA, S4)¹⁹. We then switch to finite difference time domain simulations (FDTD, Lumerical FDTD Solutions) and use the parameters (nanopillar radius, height, and unit cell size) as a starting point for fine-tuning the design for large negative GDD, low higher-order dispersion, and high transmission over an extended spectral band. The resulting compressor geometry (Fig. 2b) shows strong anomalous GDD centered at 800 nm wavelength; its phase, group delay, and transmission characteristics are shown in Fig. 1c-e. From 760 to 840 nm, the group delay deviates less than 2 fs from a group delay profile with constant anomalous GDD of -71 fs^2 . If a highly linear group delay profile is required, a stronger-dispersive regime exists between 780 and 825nm: It provides anomalous $GDD = -82 \text{ fs}^2$ with less than 0.5 fs deviation from a linear group delay profile. FDTD modeling predicts close to unity transmission over the full working range.

The response of the compressor's dispersion and transmission properties to changes of the nanopillar diameter, height, and periodicity is explored in Figs. S1 & S2. By changing the nanopillar diameter, the broadband Mie-type transverse magnetic dipole resonance²⁰ of the nanopillars can be spectrally

shifted to achieve anomalous dispersion at a desired central wavelength. By changing the nanopillar height, the magnitude of the induced anomalous dispersion can be controlled. In practice, only specific nanopillar heights can be realized because Fabry-Perot-resonances have to be accounted for to achieve high transmission. The design introduced here features an undesirable narrowband Fabry-Perot resonance within the spectral working range (see Fig. 1e). For a given nanopillar diameter and height, the periodicity of the array can be tuned to suppress this resonance (see Figs. S1 & S2) and achieve a smooth phase and transmission profile. The interaction between the narrowband Fabry-Perot and the broadband Mie-resonance is described in detail elsewhere²⁰⁻²³. The small residual signature of this resonance is inconsequential for the temporal envelope of broadband ultrashort laser pulses due to its narrow spectral width. The transmission and phase characteristics of the compressor do not change significantly for slanted incidence angles of up to 5° for s-polarized light (see Fig. S3).

To experimentally verify our design, we fabricated compressors with varying nanopillar radii by lithographic top-down processing of a 610 nm-thick amorphous silicon layer on a 0.5 mm-thick fused silica substrate (see methods), Fig. 2a shows a sample imaged using scanning electron microscopy.

Fig. 2 and Table 1 present the experimental group delay characteristics of compressors for three different nanopillar diameters, measured using white light interferometry²⁴ (see methods). The coatings induce anomalous GDD of up to -71 fs^2 over a working bandwidth of up to 80 nm around a center wavelength tunable by changing the nanopillar diameter. This suffices for compensating the GDD of 2 mm-thick fused silica glass ($\text{GDD}(\text{SiO}_2, 800 \text{ nm}) = +36.2 \text{ fs}^2/\text{mm}$)²⁵. The FDTD predictions match the experimental group delay and transmission profiles well.

We observe a residual signature of the suppressed Fabry-Perot resonance (see above). This signature limits the linear working range on the high-frequency side (see, e.g., Fig. 2d, g). However, at the same time, it increases the anomalous GDD in the linear working range to up to -128 fs^2 , (see black lines in Fig. 2d-f). The GDD magnitude of our compressor makes it about 5800 times more dispersive than glass per unit length. A broadband dip of the transmission profiles on the low-frequency side of the working range decreases the average transmission in the working range to $\sim 80\%$. This behavior is reproduced when including a 4 nm fabrication tolerance of the nanopillar diameter in the simulations. Thus, close to unity transmission should be achievable by using improved fabrication.

Table 1 Experimental compressor characterization			
nanopillar diameter [nm]	147 ± 7	158 ± 7	170 ± 6
full working range [nm]	705 - 775	740 - 810	770 - 850
avg. GDD [fs^2]	-71 ± 1	-61 ± 2	-64 ± 2

linear working range [nm]	735 - 770	775 - 805	800-840
avg. linear GDD [fs ²]	- 120 ± 2	- 128 ± 6	- 127 ± 4
full working range avg. transmission	81%	79%	80%

To demonstrate the viability of our concept in a real application, we inserted a compressor (nanopillar diameter 162 ± 6 nm) in the path of a mode-locked titanium-sapphire oscillator. To confirm the resulting changes in the femtosecond laser pulses directly in the time domain, we employ second-harmonic frequency-resolved-optical-gating²⁶ (SH-FROG, see Fig. 3f for setup and methods for details): laser pulses are split into two replicas and delayed with respect to each other. They are then non-collinearly overlapped in a nonlinear crystal. Only when the pulses traverse the crystal simultaneously, second harmonic radiation is emitted towards the detector. Thus, recording the delay-dependent second-harmonic spectrum yields a spectrogram from which the intensity and phase profiles of the laser pulses can be reconstructed. Because the second harmonic process mixes two photons from identical pulse copies, the generated spectrum $S(\tau) = S(-\tau)$ is equal for positive and negative delay time τ between the two pulse copies. Thus, SH-FROG spectrograms are symmetric with respect to the zero-delay time (see, e.g., Fig. 3a, b). Due to this symmetry, the sign of the GDD measured using SH-FROG can be ambiguous²⁷. By ensuring that the incoming pulse GDD magnitude exceeds that of the compressor, sign changes of the GDD can be avoided, thus eliminating this uncertainty.

We measured spectrograms for: i) the input laser pulses, ii) the laser pulses affected by the fused silica substrate, and iii) the laser pulses after traversing the compressor and substrate. Experimental spectrograms are displayed in Fig. 3a, b, while the full data set, retrieved spectrograms, and retrieval process are detailed in the methods and Fig. S4. Both, visual comparison of the reconstructed spectrograms (see Fig. S4) and the trace-area normalized FROG error $G' < 0.05$ ^{28,29} of the reconstructed spectrograms indicate good agreement.

In the time-domain (Fig. 3c, d), the compressor reduces the pulses' full-width-at-half-maximum duration by a quarter from (48.3 ± 1.2) fs to (37.5 ± 1.3) fs, clearly demonstrating compression although the laser bandwidth exceeds the linear compressor working range. We can relate these time-domain measurements with the group delay profiles obtained from white light interferometry up to a constant offset (Fig. 3e). Agreement within the uncertainty proves both methods are viable for the determination of the group delay properties of thin compressor coatings. Spectral domain results are summarized in Table 2, Fig. 3e, and Fig. S4. When numerically applying the measured characteristics to a light pulse matched to the full working range (Gaussian-shape, FWHM spectral bandwidth 760 nm – 840 nm) stretched from 10 fs to 19 fs by 1.6 mm-thick fused silica glass, the compressor

suppresses more than 65% of the pulse elongation and recompresses the pulse to below 13 fs. Thus, it can sufficiently compensate for the dispersion of many beam splitters, polarizers, waveplates, etc.

	Laser Pulse GDD [fs ²]			Optics GDD [fs ²]	
	incoming pulse	substrate	compressor and substrate	substrate (0.5 mm SiO ₂)	compressor
full working range 760 – 840 nm	+191 ± 5	+210 ± 4	+154 ± 4	+17 ± 6	-58 ± 6

The main working principle of the compressor can be approached from a scattering perspective^{18,20,21} or from the perspective of an array of waveguides^{30–33}. Here we follow the second approach.

We examine the dispersion of the eigenmodes of a two-dimensional compressor cross-section (i.e., the out-of-plane dispersion of the two-dimensional photonic crystal) in Fig. 4a. At near-infrared wavelengths, incoming light couples predominantly to two modes (see Fig. 4b) - with electric field profiles similar to the HE₁₁ and HE₁₂ hybrid modes in dielectric waveguides - due to their matching field symmetries (see Fig. 4c and ref. ³⁰). Light in the HE₁₁-like mode is mainly confined in the silicon nanopillars whereas it also travels in free space in the HE₁₂-like mode (see Fig. 4c). Because the compressor is large compared to its periodicity, light leaking out of a single nanopillar is not lost. Thus, the propagation constant of the HE₁₂-like mode is real above the vacuum light line (see Fig. 4a).

The anomalous GDD of our device is caused by the dispersion of the HE₁₂-like mode close to $k_z = 0$: because light must travel at the same speed in both the backward and forward direction, reciprocity requires that the group velocity $v_g = \frac{d\omega}{dk_z} \rightarrow 0^+$ of light propagating in the HE₁₂-like mode vanishes at $k_z \rightarrow 0^+$. In the absence of losses, this is true for all modes except for the fundamental mode or the special case of degenerate modes³⁴. Consequently, close to the cutoff at $k_z = 0$, the mode enters a region of slow light³⁵, which is visible in Fig. 4a as the vanishing slope of the HE₁₂-like mode dispersion. The bending of the dispersion from the vacuum light line at high frequencies into this slow light region (see arrows in Fig. 4a) creates anomalous group velocity dispersion $GVD = \frac{d^2k_z}{d\omega^2} = \frac{dv_g^{-1}}{d\omega}$ at frequencies above $k_z = 0$. If light would couple exclusively to the HE₁₂-like mode, the compressor group delay would diverge close to the $k_z = 0$ cutoff, preventing broadband operation. However, at the cutoff, light coupling rapidly shifts to the HE₁₁-like mode (see Fig. 4b). The mixing of both modes generates the broadband region of constant anomalous GDD.

We demonstrated transmissive broadband pulse-compressor nanocoatings for the important VIS-NIR spectral region, which compensate the GDD of up to 2 mm-thick fused silica glass over a bandwidth of up to 80 nm, and their application to femtosecond light pulses. Our approach can be implemented on conventional optics and requires no spatial, angular, or polarization pre-conditioning of the incoming light, therefore it can be rapidly implemented in optical setups. As group delay characteristics are determined by geometric properties, rather than material dispersion, the approach is flexible and can be adapted to different spectral regions or applications. In the future, stacked or more intricate structures tailored by inverse design or machine learning can expand the technique towards engineering complex pulse shapes for coherently controlling chemical reactions and quantum systems or optimizing nonlinear processes such as high-harmonic generation.

Methods

Fabrication

First, we deposit a 610 nm-thick amorphous silicon layer on a 500 μm -thick fused silica substrate using plasma-enhanced chemical vapor deposition. After spin-coating a layer of negative electron beam resist (Micro Resist Technology, ma-N 2403) and an additional layer of conductive polymer (Showa Denko, ESPACER 300) to avoid charging effects during electron beam lithography (EBL), we define the nanopillar mask patterns using EBL (Elionix, ELS-F125) and develop (MicroChemicals, MIF 726). Anisotropic inductively coupled plasma-reactive ion etching (ICP-RIE using a mixture of SF₆ and C₄F₈) was used to etch the nanopillar structures. The electron beam resist mask was removed by immersing the sample in piranha solution.

White light interferometry

We determine the group delay profiles of our compressors using a self-built white light interferometer. Broadband black body radiation from a tungsten lamp (Thorlabs SLS202L) is coupled to a multimode fiber, then collimated and linearly polarized before a Michelson interferometer. In the interferometer, light in one arm is used as reference and is delayed, light in the other arm is modified by the sample. After the interferometer, the spectral interference between light from both arms is resolved using an Andor Shamrock spectrometer and reveals the group delay profile of the sample.

Femtosecond Oscillator, FROG Measurements and Retrieval

Measurements were performed on the uncompressed output of a Femtosecond Rainbow (FEMTOLASERS Produktions GmbH) femtosecond oscillator using a self-built noncollinear SH-FROG. The uncompressed pulses are elongated by the GDD and third order dispersion of the oscillator, a

fused silica lens, beam splitter and air path (spectral phase of the incoming pulses see Fig. S4j). In the time domain (Fig. S4g), the GDD causes a symmetric broadening, whereas the third order dispersion causes the substructure³⁶⁻³⁸. The group delay profile shown in Fig. 3e is determined by subtracting the group delay profiles in Fig. S4 k and l. Because these were both measured using the same incoming laser pulses, the subtraction eliminates the group delay profiles of the incoming laser pulses. We employ a self-written retrieval algorithm based on the iterative ptychographic engine³⁹ to retrieve the pulse characteristics (Fig. S4g-l) from the experimental spectrograms (Fig. S4a-c). We correct for the phase matching conditions in our 100 μm thick beta-barium-borate crystal before the retrieval and ignore non-phase-matched spectral components during the retrieval (see Fig. S4a-c). To increase the accuracy of the retrieval, we use the measured power spectrum of the fundamental laser pulses as an additional constraint during the retrieval. This approach was shown to retrieve correct temporal and spectral pulse properties, even for incomplete spectrograms³⁹. In our case, it provides reliable spectral information even in the non-phase-matched spectral ranges of the ultrashort pulses, witnessed by the excellent agreement between the compressor's group delay profile measured using the SH-FROG and white-light interferometry (Fig. 3e). Spectrograms calculated from the retrieved pulse parameters are displayed in (Fig. S4d-f) for comparison. Errors were determined using the bootstrap method⁴⁰.

Acknowledgments

This work was performed, in part, at the Center for Nanoscale Systems (CNS), a member of the National Nanotechnology Coordinated Infrastructure (NNCI), which is supported by the NSF under award no. ECCS-2025158. CNS is a part of Harvard University. M.O. acknowledges a Feodor-Lynen Fellowship from the Alexander von Humboldt Foundation. Z.W. acknowledges funding by the China Scholarship Council (201906180074).

Author contributions

M. O., W.-T. C., Y. A. I., X. Y.: simulation.

Y.-W. H.: fabrication.

M. O., Z. W.: experimentation.

M. O., X. Y.: data analysis.

M. O., M. S., F. C.: writing.

F. C.: supervision.

All authors discussed the manuscript.

References

1. Zipfel, W. R., Williams, R. M. & Webb, W. W. Nonlinear magic: multiphoton microscopy in the biosciences. *Nat. Biotechnol.* **21**, 1369–1377 (2003).
2. Soong, H. K. & Malta, J. B. Femtosecond Lasers in Ophthalmology. *Am. J. Ophthalmol.* **147**, 11 (2009).
3. Gattass, R. R. & Mazur, E. Femtosecond laser micromachining in transparent materials. *Nat. Photonics* **2**, 219–225 (2008).
4. Zewail, A. H. Femtochemistry: Atomic-Scale Dynamics of the Chemical Bond. *J. Phys. Chem. A* **104**, 5660–5694 (2000).
5. Fork, R. L., Martinez, O. E. & Gordon, J. P. Negative dispersion using pairs of prisms. *Opt. Lett.* **9**, 150 (1984).
6. Strickland, D. & Mourou, G. Compression of amplified chirped optical pulses. *Opt. Commun.* **56**, 219–221 (1985).
7. Meshulach, D. & Silberberg, Y. Coherent quantum control of multiphoton transitions by shaped ultrashort optical pulses. *Phys. Rev. A* **60**, 1287–1292 (1999).
8. Mayer, E. J., Möbius, J., Euteneuer, A., Rühle, W. W. & Szipőcs, R. Ultrabroadband chirped mirrors for femtosecond lasers. *Opt. Lett.* **22**, 528 (1997).
9. Kärtner, F. X. *et al.* Ultrabroadband double-chirped mirror pairs for generation of octave spectra. *J. Opt. Soc. Am. B* **18**, 882 (2001).
10. Pervak, V., Ahmad, I., Trubetskov, M. K., Tikhonravov, A. V. & Krausz, F. Double-angle multilayer mirrors with smooth dispersion characteristics. *Opt. Express* **17**, 7943 (2009).
11. Knight, J. C. *et al.* Anomalous dispersion in photonic crystal fiber. *IEEE Photonics Technol. Lett.* **12**, 807–809 (2000).
12. Kamali, S. M., Arbabi, E., Arbabi, A. & Faraon, A. A review of dielectric optical metasurfaces for wavefront control. *Nanophotonics* **7**, 1041–1068 (2018).
13. Khorasaninejad, M. & Capasso, F. Metalenses: Versatile multifunctional photonic components. *Science* **358**, eaam8100 (2017).
14. Staude, I. & Schilling, J. Metamaterial-inspired silicon nanophotonics. *Nat. Photonics* **11**, 274–284 (2017).
15. Shaltout, A. M., Shalaei, V. M. & Brongersma, M. L. Spatiotemporal light control with active metasurfaces. *Science* **364**, eaat3100 (2019).
16. Divitt, S., Zhu, W., Zhang, C., Lezec, H. J. & Agrawal, A. Ultrafast optical pulse shaping using dielectric metasurfaces. *Science* **364**, 890–894 (2019).
17. Rahimi, E. & Şendur, K. Femtosecond pulse shaping by ultrathin plasmonic metasurfaces. *J. Opt. Soc. Am. B* **33**, A1 (2016).
18. Decker, M. *et al.* High-Efficiency Dielectric Huygens' Surfaces. *Adv. Opt. Mater.* **3**, 813–820

(2015).

19. Liu, V. & Fan, S. S4 : A free electromagnetic solver for layered periodic structures. *Comput. Phys. Commun.* **183**, 2233–2244 (2012).
20. Abujetas, D. R., Mandujano, M. A. G., Méndez, E. R. & Sánchez-Gil, J. A. High-Contrast Fano Resonances in Single Semiconductor Nanorods. *ACS Photonics* **4**, 1814–1821 (2017).
21. Bogdanov, A. A. *et al.* Bound states in the continuum and Fano resonances in the strong mode coupling regime. *Adv. Photonics* **1**, 1 (2019).
22. Limonov, M. F. Fano resonances in photonics. *Nat. Photonics* **11**, 12 (2017).
23. Cordaro, A. *et al.* Antireflection High-Index Metasurfaces Combining Mie and Fabry-Pérot Resonances. *ACS Photonics* **6**, 453–459 (2019).
24. Hlubina, P., Ciprian, D., Lunáček, J. & Lesnák, M. Dispersive white-light spectral interferometry with absolute phase retrieval to measure thin film. *Opt. Express* **14**, 7678 (2006).
25. Malitson, I. H. Interspecimen Comparison of the Refractive Index of Fused Silica. *J. Opt. Soc. Am.* **55**, 1205 (1965).
26. DeLong, K. W., Trebino, R., Hunter, J. & White, W. E. Frequency-resolved optical gating with the use of second-harmonic generation. *J. Opt. Soc. Am. B* **11**, 2206 (1994).
27. DeLong, K. W., Kohler, B., Wilson, K., Fittinghoff, D. N. & Trebino, R. Pulse retrieval in frequency-resolved optical gating based on the method of generalized projections. *Opt. Lett.* **19**, 2152 (1994).
28. Scott, R. P. *et al.* High-fidelity line-by-line optical waveform generation and complete characterization using FROG. *Opt. Express* **15**, 9977 (2007).
29. Jafari, R., Jones, T. & Trebino, R. 100% reliable algorithm for second-harmonic-generation frequency-resolved optical gating. *Opt. Express* **27**, 2112 (2019).
30. Fountaine, K. T., Whitney, W. S. & Atwater, H. A. Resonant absorption in semiconductor nanowires and nanowire arrays: Relating leaky waveguide modes to Bloch photonic crystal modes. *J. Appl. Phys.* **116**, 153106 (2014).
31. Ko, Y. H. & Magnusson, R. Wideband dielectric metamaterial reflectors: Mie scattering or leaky Bloch mode resonance? *Optica* **5**, 289 (2018).
32. Abujetas, D. R., Paniagua-Domínguez, R. & Sánchez-Gil, J. A. Unraveling the Janus Role of Mie Resonances and Leaky/Guided Modes in Semiconductor Nanowire Absorption for Enhanced Light Harvesting. *ACS Photonics* **2**, 921–929 (2015).
33. Tong, L., Lou, J. & Mazur, E. Single-mode guiding properties of subwavelength-diameter silica and silicon wire waveguides. *Opt. Express* **12**, 1025 (2004).
34. Huang, X., Lai, Y., Hang, Z. H., Zheng, H. & Chan, C. T. Dirac cones induced by accidental degeneracy in photonic crystals and zero-refractive-index materials. *Nat. Mater.* **10**, 582–586 (2011).
35. Baba, T. Slow light in photonic crystals. *Nat. Photonics* **2**, 465–473 (2008).
36. Trebino, R. *Frequency-Resolved Optical Gating: The Measurement of Ultrashort Laser Pulses. Frequency-Resolved Optical Gating: The Measurement of Ultrashort Laser Pulses* (Springer US, 2000).

doi:10.1007/978-1-4615-1181-6.

37. Miranda, M., Fordell, T., Arnold, C., L'Huillier, A. & Crespo, H. Simultaneous compression and characterization of ultrashort laser pulses using chirped mirrors and glass wedges. *Opt. Express* **20**, 688 (2012).
38. Lytle, A. L. *et al.* Use of a simple cavity geometry for low and high repetition rate modelocked Ti:sapphire lasers. *Opt. Express* **12**, 1409 (2004).
39. Sidorenko, P., Lahav, O., Avnat, Z. & Cohen, O. Ptychographic reconstruction algorithm for frequency-resolved optical gating: super-resolution and supreme robustness. *Optica* **3**, 1320 (2016).
40. Wang, Z., Zeek, E., Trebino, R. & Kvam, P. Determining error bars in measurements of ultrashort laser pulses. *J. Opt. Soc. Am. B* **20**, 2400 (2003).

Figures

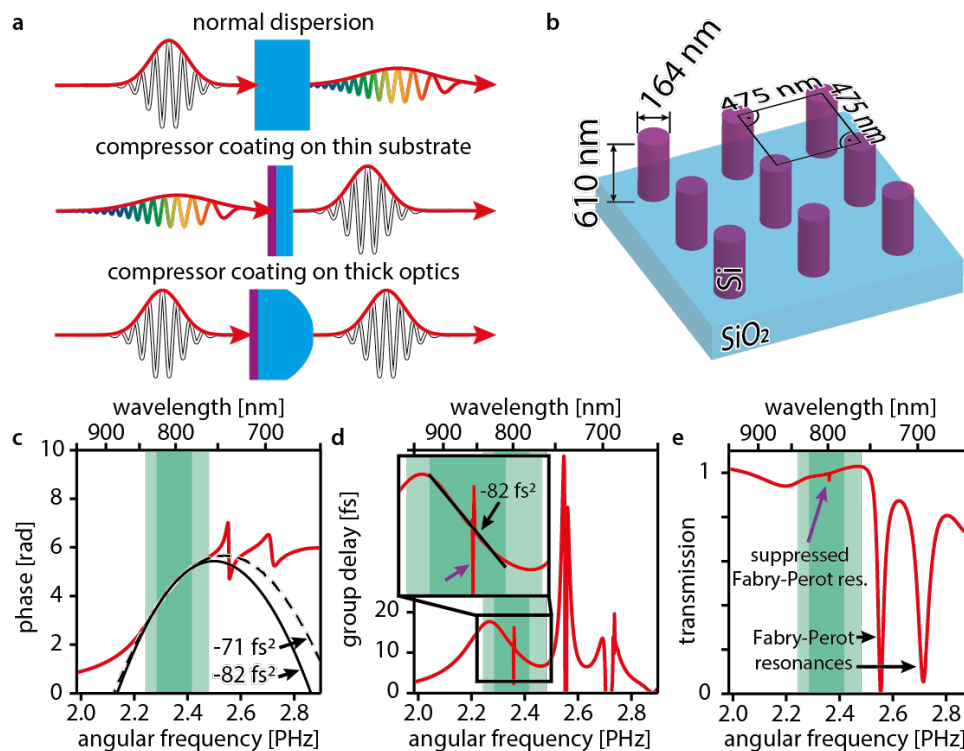


Fig. 1.

Nanocoating compressor working principle and design.

a) Chromatic dispersion effect on ultrashort laser pulses in transparent materials and possible coating applications. Short pulses are marked in white, pulses stretched by material dispersion in colors; normally dispersive materials (light blue) elongate short pulses. The coating (purple) can either be applied to a thin substrate to shorten elongated pulses or to a thick optics to compensate its group delay dispersion.

b) Design optimized for operation at 800 nm wavelength.

c) Transmission phase profile (red line) predicted by finite difference time domain (FDTD) simulations for the compressor of panel b). The dashed black line is a parabolic fit to the phase profile within the full working range (light green area) and the solid black line is a parabolic fit to the phase profile within the linear working range (dark green area). The fits are labeled with the curvatures of the parabolae, which is the group delay dispersion. The downward curvature of the parabolae indicates anomalous dispersion.

d) Simulated transmission group delay profile (red line), i.e., the derivative of the transmission phase profile. The inset shows the magnified working ranges. The black line represents a linear fit to the linear working range (dark green area) and is labeled by its group delay dispersion. The downward

slope indicates anomalous dispersion. In the full working range (light green region), the group delay deviates by less than two femtoseconds from a linear profile. A narrowband (< 1 nm) residual signature of the suppressed Fabry-Perot resonance in the working range is marked with a purple arrow in panels d & e (see text and Figs. S1 & S2).

e) Simulated transmission characteristics (red line). The working ranges (green areas) are marked as a guide to the eye.

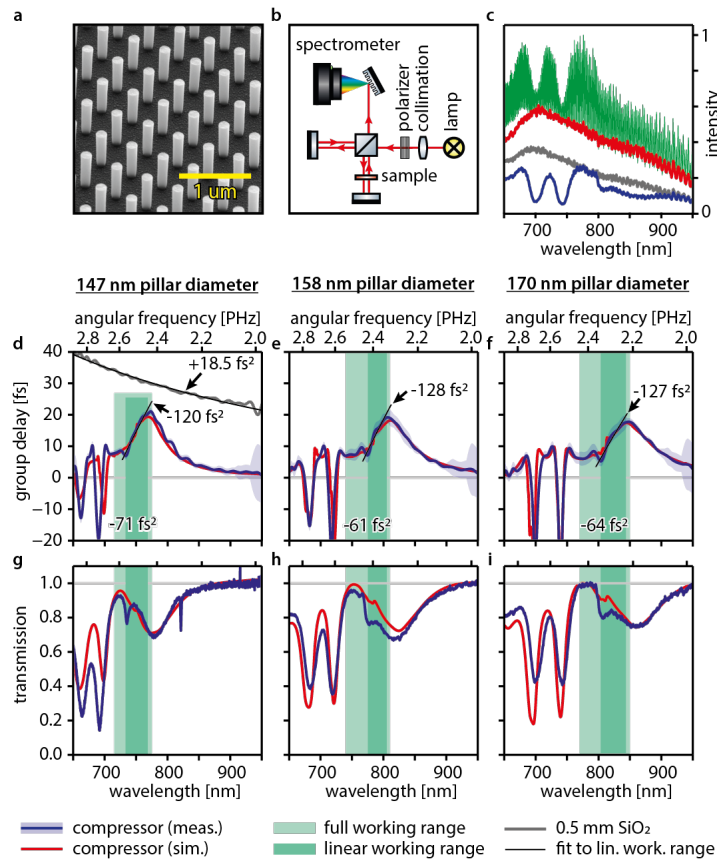


Fig. 2.

White light interferometry of compressors designed for different operating wavelengths. Samples are labeled by the nanopillar diameter.

a) scanning electron microscope picture of the compressor with 158 nm nanopillar diameter.

b) white light interferometer setup. Thermal radiation from a tungsten lamp (red lines) is collimated, polarized, and then split in a Michelson interferometer. Light in one interferometer arm passes the sample twice, light in the other arm is delayed. The variable delay between the two arms causes spectral intensity oscillations associated with the compressor group delay dispersion that are recorded by a grating spectrometer.

c) example of white light interferometer raw data for the sample with 170 nm nanopillar diameter. Interference spectrum (green); spectrum transmitted by the compressor when the reference arm is blocked (blue) and when the compressor sample is replaced by a fused silica substrate and the reference arm is blocked (grey); spectrum of the lamp, when the sample arm is blocked (red).

d-f) compressor group delay profile measured by white-light interferometry (blue lines). FDTD simulations (red lines) account for 4 nm nanopillar diameter fabrication tolerance. The black lines are linear fits to the measured group delay profiles in the linear working ranges (dark green areas) and are labeled with their group delay dispersion (slope). The average group delay dispersions in the full working ranges (light green areas) are also indicated. The measured group delay profile of the fused silica substrate (grey line) and a fit to it (black line) are shown for reference. Both were shifted vertically to fit the plotting region. The blue shaded areas represent the measurement uncertainty: To retrieve an upper bound for the systematic error, we compare a reference measurement on the fused silica substrate with its literature group delay profile. We then use the maximum deviation of the two in a 50 nm bandwidth around each wavelength point as uncertainty and add the standard deviation. g-i) measured (blue lines) and simulated (red lines) compressor transmission characteristics relative to the fused silica substrate transmission.

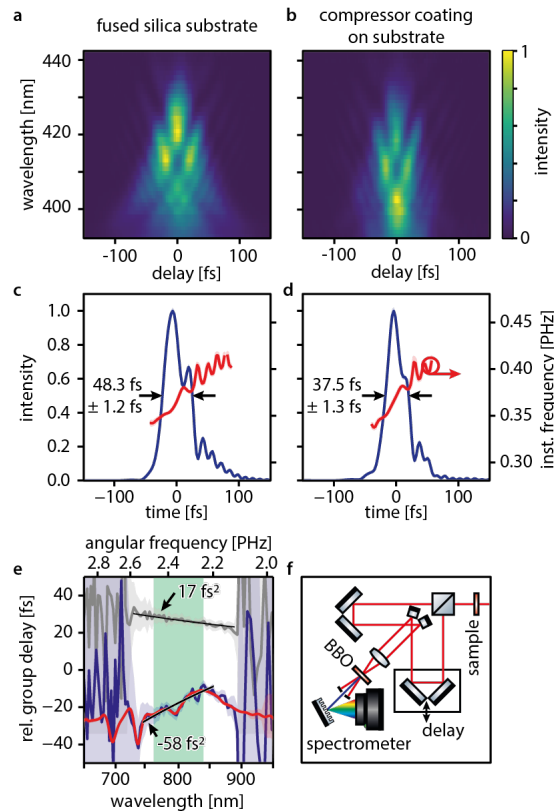


Fig. 3.

Compression of an ultrashort laser pulse.

a - b) experimental second harmonic frequency resolved optical gating (SH-FROG) spectrograms recorded after the incoming laser pulses are transmitted a) through the fused silica substrate only and b) through the compressor-coated substrate (nanopillar diameter 162 nm).

c) time domain intensity (blue line) and instantaneous frequency profiles (red line) of the laser pulses transmitted through the fused silica substrate retrieved using an iterative ptychographic reconstruction algorithm (see methods). The arrows indicate the pulse full width at half maximum duration. Standard deviations (blue and red shaded areas) were determined using the bootstrap method (see methods).

d) time domain intensity (blue line) and instantaneous frequency profiles (red line) of the laser pulses transmitted through the compressor-coated substrate. The measured full width at half maximum durations show the pulse shortening by 11 fs

e) group delay profile retrieved from the SH-FROG measurements (SH-FROG measurement: blue line, white-light interferometer measurement of the same sample: red line) and least-squares fit

(black line) to the data in the full working range (light green area). The group delay profile retrieved for the fused silica substrate (SH-FROG measurement: grey line) is displayed as a reference.

f) SH-FROG setup. The incoming laser pulses (red lines) are modified by the sample, split and delayed by the arms of an interferometer and subsequently focused and overlapped noncollinearly in a beta-Barium-Borate (BBO) crystal. Second harmonic radiation (blue line) generated by combining one photon from each arm is detected in a grating spectrometer for different delay times and reveals the temporal structure of the laser pulses.

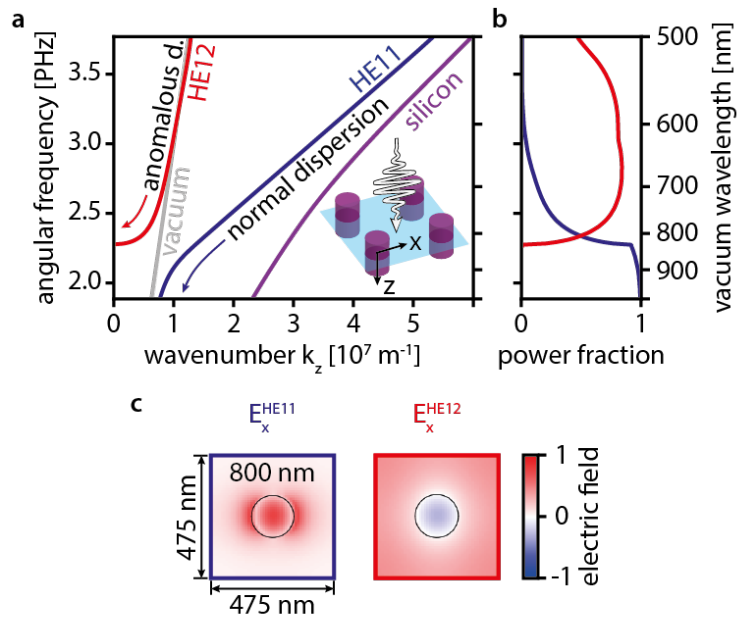


Fig. 4.

Slow-light-compressor operating principle.

a) dispersion of the predominant modes calculated for a two-dimensional cross-section (illustrated in the inset) perpendicular to the light propagation direction. The modes are labeled with the names of hybrid fiber modes with the same symmetry (HE11-like: blue line), HE12-like: red line). The vacuum (grey line) and silicon dispersions (purple line) are also plotted. One should note that the HE12-like mode's propagation constant is real above the vacuum line because light leaking out of a single nanopillar is not lost from the array. The mode's wavevector along the propagation direction vanishes at 2.3 PHz (825 nm) angular frequency ($k_z = 0$). As this cutoff is approached, the group velocity decreases (slow light), creating a region with anomalous group velocity dispersion.

b) power coupling fraction from free space to the HE11-like and HE12-like modes. The transition from light propagating in the HE12-like to the HE11-like mode at 2.3 PHz (825 nm) increases the working bandwidth

c) transverse electric field distributions of the modes at 800 nm wavelength. Whereas the HE11-like mode has no inflection points, the HE12-like mode has one inflection point.

Supplementary Figures

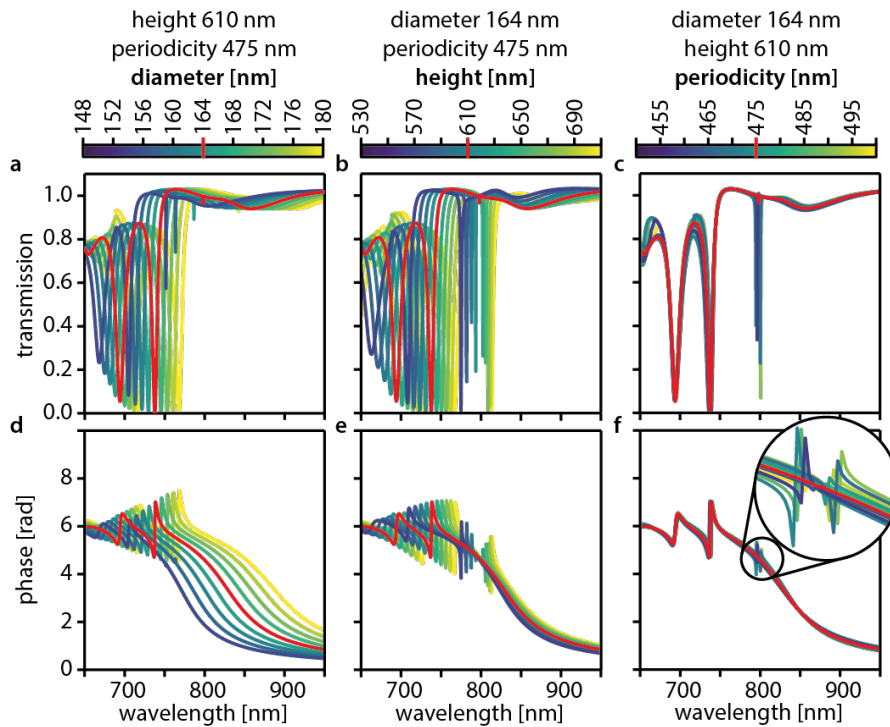


Fig. S1

Compressor response to changes in the nanopillar diameter, height, and periodicity. The optimal design for 800 nm central wavelength is marked in red.

Compressor transmission characteristics for

- a) different nanopillar diameters,
- b) heights, and
- c) periodicities.

Compressor phase profiles for

- d) different nanopillar diameters,
- e) heights, and
- f) periodicities.

Panel d) illustrates how the anomalous dispersion region can be tuned by changing the nanopillar diameter. Panels b), c), e), and f) show how the unwanted narrowband resonance at the center of the anomalous dispersion region can be avoided by selecting the correct nanopillar height and periodicity.

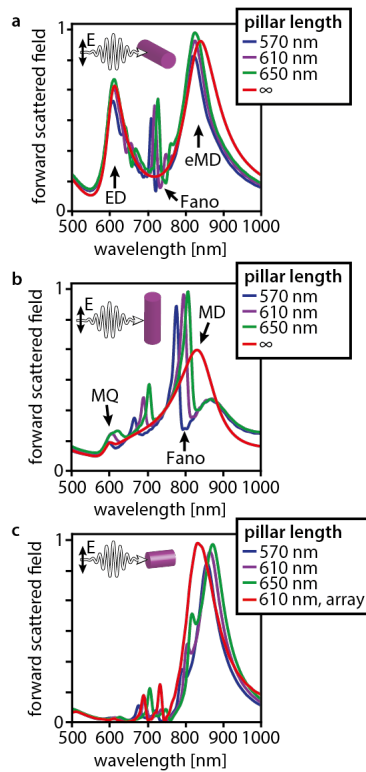


Fig. S2

Identification of Mie and Fabry-Perot resonances via forward-scattered field calculations for an individual nanopillar with 164 nm diameter and different nanopillar height.

a) forward scattering behavior for light incident perpendicular to the nanopillar with the electric field oriented perpendicular to the nanopillar (see inset). For an infinitely long nanopillar (red line), only the Mie-type longitudinal magnetic dipole (eMD) and electric dipole (ED) resonance are visible. For finite nanopillar length, narrow Fabry-Perot-type resonances appear that spectrally shift when changing the nanopillar length. They show a strong Fano-type interaction with the broadband Mie-type resonances.

b) forward scattering behavior for light incident perpendicular to the nanopillar with the electric field oriented along the nanopillar. For an infinitely long nanopillar (red line), only the Mie-type broadband transverse magnetic dipole (MD) and magnetic quadrupole (MQ) resonance are visible. For finite nanopillar length, narrowband Fabry-Perot-type resonances appear that also show a strong Fano-type interaction with the broadband Mie-type resonances.

c) The Fano-type interaction between the Mie-type and Fabry-Perot-type resonances displayed in panel b) is also visible in the forward scattering behavior of an individual nanopillar when light is incident along the nanopillar axis. Arranging the nanopillars in a 475 nm x 475 nm array (red line) suppresses the interaction.

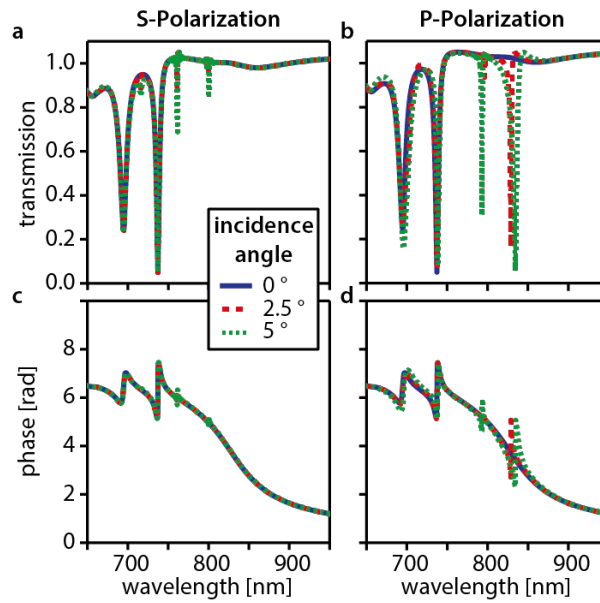


Fig. S3

Compressor response (164 nm pillar diameter, 610 nm pillar height, 475 nm periodicity) to different angles of light incidence.

Compressor transmission characteristics for

a) incident light with s-polarization and

b) p-polarization.

Compressor phase profiles for

c) incident light with s-polarization and

d) p-polarization.

For s-polarized light, both, the transmission and phase of the compressor are robust against slanted incidence. For p-polarized light, slanted incidence reduces the long-wavelength limit of the working range.

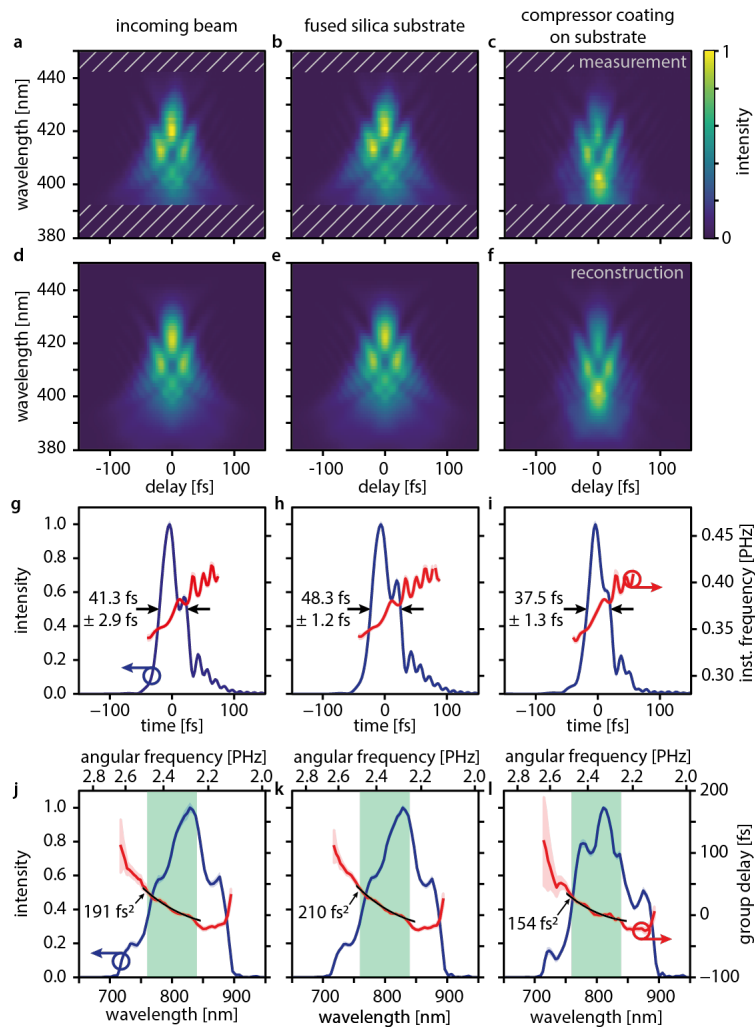


Fig. S4.

Compression of ultrashort laser pulses, full data set.

a - c) experimental second harmonic frequency resolved optical gating spectrograms (SH-FROG) of the incoming laser pulses (1st column), the pulses after transmission through the compressor substrate only (2nd column), and the pulses after the compressor (3rd column). Hatched areas are not phase-matched and were not used for reconstruction.

d-f) spectrograms reconstructed using the iterative ptychographic reconstruction algorithm.

g-i) measured time domain intensity (blue lines) and instantaneous frequency (red lines) profiles.

Standard deviations were determined using the bootstrap method (blue and red shaded areas). The arrows and labels indicate the pulse full width at half maximum duration.

j-l) measured spectral domain intensity (blue lines) and group delay (red lines) profiles and least-squares fits (black lines) to the group delay profiles in the working range (light green). Fits account for 300 fs^3 third order dispersion of the incoming pulses and are labeled with their slope, i.e., group delay dispersion of the laser pulses.